nature ecology & evolution

ARTICLES

https://doi.org/10.1038/s41559-017-0371-8

A mesic maximum in biological water use demarcates biome sensitivity to aridity shifts

Stephen P. Good[1]*, Georgianne W. Moore[2] and Diego G. Miralles[3]

Biome function is largely governed by how efficiently available resources can be used and yet for water, the ratio of direct biological resource use (transpiration, E_T) to total supply (annual precipitation, P) at ecosystem scales remains poorly characterized. Here, we synthesize field, remote sensing and ecohydrological modelling estimates to show that the biological water use fraction (E_T/P) reaches a maximum under mesic conditions; that is, when evaporative demand (potential evapotranspiration, E_P) slightly exceeds supplied precipitation. We estimate that this mesic maximum in E_T/P occurs at an aridity index (defined as E_P/P) between 1.3 and 1.9. The observed global average aridity of 1.8 falls within this range, suggesting that the biosphere is, on average, configured to transpire the largest possible fraction of global precipitation for the current climate. A unimodal E_T/P distribution indicates that both dry regions subjected to increasing aridity and humid regions subjected to decreasing aridity will suffer declines in the fraction of precipitation that plants transpire for growth and metabolism. Given the uncertainties in the prediction of future biogeography, this framework provides a clear and concise determination of ecosystems' sensitivity to climatic shifts, as well as expected patterns in the amount of precipitation that ecosystems can effectively use.

Given the widespread changes in climate and land use patterns currently underway[1,2], the estimation of future biogeochemical cycles requires an understanding of how efficiently biomes use local resources[3], how the availability of these resources may be altered[4] and also how resource-use efficiencies may be altered moving forward[5]. Water and carbon—key resources required throughout the biosphere—are principally linked through stomatal exchange, as the majority of water taken up by plants is lost through transpiration during photosynthesis. Accordingly, the net primary production (NPP) of ecosystems is known to peak in high precipitation tropical regions[6], yet rainfall use efficiency (the ratio of NPP/P) has been observed to decrease with increasing rainfall[7]. Field studies show a decrease in transpiration as rainfall becomes very large (for example, above 3,000 mm yr^{-1}; Supplementary Fig. 1). This decline is attributed to sub-optimal conditions for photosynthesis and transpiration driven by factors such as lower atmospheric evaporative demand associated with elevated cloud cover, waterlogged soils associated with reduced nutrient cycling and the film of intercepted water on leaves blocking gas exchange[8–10]. However, temperature complicates this productivity–rainfall interaction, as aboveground NPP declines occur primarily in cool, but not warm, tropical forests[11]. Additional research across biomes indicates that grassland NPP is highest at intermediate, and not large, precipitation amounts[12].

In addition to annual precipitation totals, other factors are known to influence ecosystem productivity and water use. Soil texture determines the holding capacity of the rooting zone, and low precipitation grasslands (<370 mm yr^{-1}) in sandy soils are more productive than grasslands in loamy soils, while the opposite is true when precipitation increases (>370 mm yr^{-1})[13]. The vertical distribution of roots within the soil column has also been positively correlated with productivity, as more diverse deeper-rooted ecosystems have access to greater volumes of precipitation[14]. Intra-annual precipitation variability also influences ecosystems in significant ways and African locations with similar precipitation totals but more intense individual events have lower fractional woody cover[15]. While all ecosystems respond to changes in hydroclimate conditions, analysis of tree rings suggests that both arid and humid regions respond to drought at shorter time scales than semi-arid and semi-humid regions[16]. Eddy covariance observations show a contrasting response in the ratio of gross primary production (GPP) to actual evapotranspiration (E_A) between arid (GPP/E_A increases with drought) and semi-arid or sub-humid (GPP/E_A decreases with drought) regions[17]. Taken together, these results suggest complex, nonlinear interactions between ecosystem function and the hydrological cycle, indicating that not only are dryland ecosystems sensitive to and shaped by water availability[3], but wet regions may be similarly sensitive to shifts in precipitation associated with climate change[18,19]. Finally, while trends in carbon fluxes (for example, NPP and GPP) have been shown to be nonlinear with precipitation across scales, the way in which biological water use varies with respect to hydroclimate remains poorly understood.

Linking biological water demands with atmospheric water supplies can be achieved through quantification of the fraction of precipitation used by vegetation; that is, E_T/P. Attempts to partition the total surface-to-atmosphere water flux (E_A) into its constituents of canopy interception (E_I), plant transpiration and ground surface evaporation (E_S) have involved primarily in situ estimates[20,21], but have also recently been implemented on a global scale using stable isotopes[22] and remote sensing approaches[23]. A variety of mechanisms have been proposed to explain transpiration patterns, including relationships between transpiration and seasonality[21], precipitation totals[20], vegetation cover[24], leaf area index[25], latitude[26] and connections with groundwater[27], yet no consensus has been reached. However, transpiration is broadly understood to make up the majority of the global surface-to-atmosphere vapour flux, although landscape disturbance and conversion can lower the maximum transpiration at a given location[28] and the interactions

[1]Department of Biological and Ecological Engineering, Oregon State University, Corvallis, OR, USA. [2]Department of Ecosystem Science and Management, Texas A&M University, College Station, TX, USA. [3]Laboratory of Hydrology and Water Management, Ghent University, Ghent, Belgium. *e-mail: stephen.good@oregonstate.edu

between soil moisture availability, vegetation structure and plant water use have not yet been fully elucidated.

A mesic maximum in biological water use

A first-order approach to partitioning precipitation into runoff and non-runoff losses is provided by the Budyko framework[29], which has served as a cornerstone of hydrological science for decades. The fundamental advance in Budyko's approach is that the fraction of precipitation returning to the atmosphere (E_A/P) has two theoretical upper bounds under equilibrium conditions: an energy limit ($E_A \leq E_p$) and a water limit ($E_A \leq P$). When plotted against ecosystem aridity (E_p/P), undisturbed biomes generally fall along a single smooth E_p/P curve below these two bounds, such that runoff ($Q = P - E_A$) can be readily estimated given aridity (Supplementary Fig. 2) and precipitation. Based on a compilation of field observations, we show here that E_T/P also generally falls along a single unimodal curve (Fig. 1a) constrained by inherent limits on transpiration under both xeric and hydric climates. As such, we propose that a 'mesic maximum' occurs in the biological water use fraction and refine ecohydrological partitioning within the context of the Budyko framework.

We identify this mesic maximum in E_T/P based on three primary lines of evidence: field studies, remotely sensed estimates and a minimalistic ecohydrological model. Field studies using a variety of methods, such as sap flow sensors, lysimeters and isotope techniques, demonstrate low values in the E_T/P ratio at both low and high aridity levels (Fig. 1a). These studies span a wide variety of biomes, from cloud forest to deserts, and represent the range of aridity values found globally. The highest E_T/P value of 0.81 in these studies occurs in a lowland rainforest with an aridity value of 1.4 (see Supplementary Table 1). However, we acknowledge that it is a challenge to ascribe precisely the value of aridity at which this peak occurs, given the wide assortment of experimental methods, observation techniques and limited spatial coverage.

To reinforce the sparse coverage of field studies relative to the total continental surface, we also examine the E_T/P ratio based on three primary remote sensing algorithms, which are dedicated to estimating global evapotranspiration and the partitioning of this flux. These three approaches—the MODIS Penman–Monteith (PM-MOD) algorithm, Global Land Evaporation Amsterdam Model (GLEAM) and Jet Propulsion Laboratory Priestley–Taylor (PT-JPL) algorithm—all employ different methodologies to estimate transpiration based on available remote sensing observations of its biophysical drivers[23]. Despite the differences in these approaches and in their estimates of total transpiration, all three demonstrate similar unimodal distributions in E_T/P ratios (Fig. 1b), with the mesic maxima occurring at aridity values of 2.4, 1.7 and 2.6 for PM-MOD, GLEAM and PT-JPL, respectively.

A third line of evidence is provided by extending a widely used ecohydrological modelling approach. The minimalistic approach of Porporato et al.[30] used dimensional analysis based on climate forcing, soil properties and vegetation structure to analytically derive a near-identical match to the empirically derived Budyko's curve for E_A/P. Here, this model is extended (see Methods) to partition actual evapotranspiration into ground surface evaporation, transpiration and interception relative to total precipitation (Fig. 1c) or total evapotranspiration flux (Supplementary Fig. 3). Using hydraulic properties of a sandy loam soil[31], canopy interception amounts of 15% of precipitation[32], average storm depths of 7.4 mm (ref. [33]) and average rooting depths of 67.8 cm (ref. [34]), this model provides an excellent fit to measured E_T/P ratios across multiple orders of magnitude in aridity (dashed lines in Fig. 1a,b and Supplementary Fig. 4). While many of the minimalistic model inputs (rooting depth, rainfall climatology and so on) vary significantly in space, parameterization with site-specific values requires downscaling and/or interpolation of datasets with large uncertainties; hence, we conservatively apply our model with average global values here. This simple model using average global values of dimensionless constants has a root-mean-square error of 0.13 in predicted E_T/P across 45 studies ($r^2 = 0.57$, probabilty value « 0.01). The resulting curve reaches its maximum value at $E_p/P = 1.9$ and falls within the envelope of remote-sensing-based estimates.

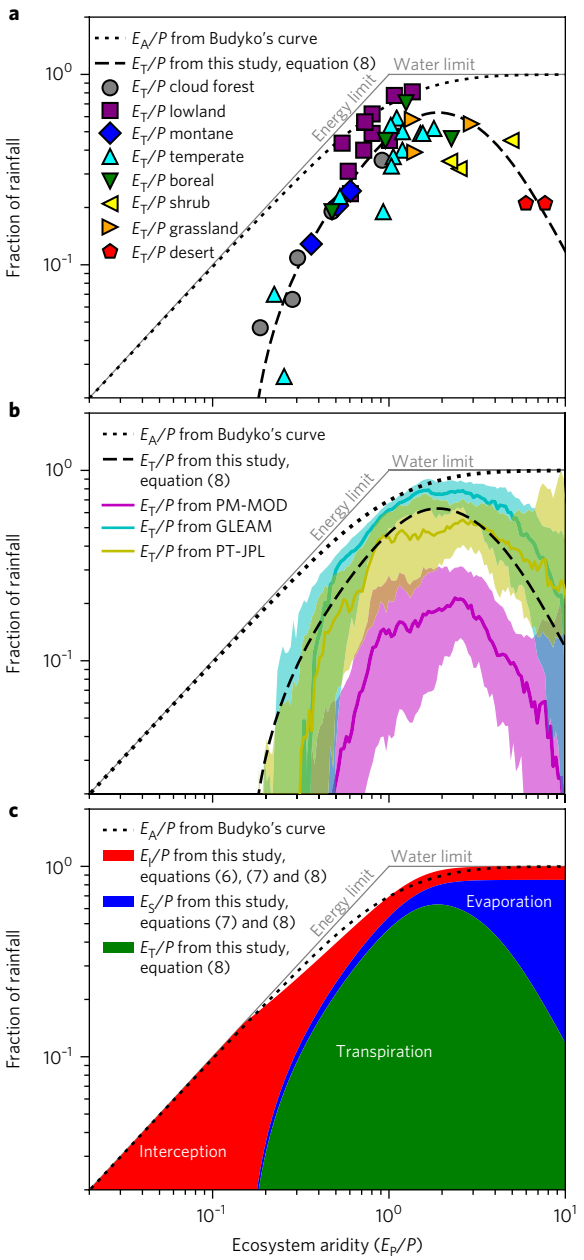

Fig. 1 | Transpired fraction of rainfall. a, Field studies of the biological water use fraction plotted with respect to aridity. See Supplementary Table 1 for classification of the field studies. **b**, Remote-sensing-based estimates of the biological water use fraction from the PM-MOD algorithm, GLEAM and the PT-JPL algorithm[23]. **c**, Modelled partitioning of rainfall based on a minimalistic model (see Methods). The dashed line in **a** and **b** traces the same region as the green area in **c** and the dotted line in **a**, **b** and **c** is Budyko's curve[29] for E_A/P.

Implications for current and future biomes

Fundamentally, arid regimes where potential evapotranspiration greatly exceeds precipitation are subject to large losses from ground

surface evaporation before vegetation can take up any available water and thus the sparse coverage of plants in dry ecosystems arises due to the limited amount of water they are able to pass through their stomata. On the wet end of the spectrum, when precipitation greatly exceeds potential evapotranspiration, little energy is available to vapourize water relative to the total volume and most precipitation exits as runoff. Furthermore, as canopies intercept precipitation before it reaches soils, a wet layer forms on leaves that inhibits leaf gas exchange[10] and a large fraction of incident energy is consumed during vapourization of this water.

The aridity value where E_T/P reaches its maximum varies with rainfall patterns, vegetation structure and soils properties and can be constrained based on our minimalistic model. After evaluation of a wide suite of possible climate, soil and vegetation configurations, the aridity regime at which the mesic maximum occurs has an average value of $E_p/P = 1.5$, with an interquartile range of 1.3 to 1.9 across all simulations. The peak consistently falls near the intersection of global average aridity[35], which is an E_p/P value of ~1.8, and the global average rooting strategy, which is represented here as the ratio of mean storm depth[33] to effective root depth[34] (see magenta lines in Fig. 2a). This suggests that on a global scale plants allocate only enough roots to capture supplied water, allowing them to maximize E_T/P near the current average global aridity—a conclusion that is both unsurprising and worrisome as aridity patterns change[1,2]. Similarly, the magnitude of E_T/P at the mesic maximum also varies with climate, soils and vegetation structure. Across the tested parameter space, a clear sigmoidal relationship becomes evident (Fig. 2b), with the observed global ratio of storm depth to rooting depth occurring near the upper inflection point (magenta line Fig. 2b). This also suggests that, on average, further investment in root growth by plants in undisturbed biomes is not likely to result in appreciably more transpiration.

Given global aridity levels[35] (Fig. 3a), the presence of a mesic maximum in E_T/P is intuitive and provides a simple, first-order prediction of how soils, vegetation and climate interact to partition rainfall (Fig. 3b). In addition, it is also directly useful for predictions of future hydroclimate and biogeography. The local slope of the derived E_T/P curve of Fig. 1, $\partial(E_T/P)/\partial(E_p/P)$, describes the sensitivity of the biological component of the hydrological cycle to altered aridity at each value of E_p/P and is mapped globally (Fig. 3c). Because of the unimodal nature of the E_T/P curve, more arid conditions locally are expected to cause a decrease (or increase) in the fraction of precipitation that is transpired if the ecosystem currently has an E_p/P value larger (or smaller) than that where the mesic maximum occurs.

The aridity value of the mesic maximum thus demarcates regions that would be positively and negatively impacted by an increase in local aridity. Regions that are most vulnerable are locations with the steepest slopes in the E_T/P versus E_p/P curve. A common yet actively debated summary of the effects of climate change on the hydrological cycle is that accelerated moisture transport drives wet-gets-wetter/dry-gets-drier shifts in climate[2,36–38]. If so, our results predict that many temperate, tropical and high-latitude forested ecosystems will suffer decreases in their transpiration ratio as their aridity decreases, while many grassland and savanna regions will also see decreases in their transpiration ratio as they are exposed to more arid conditions. Future predictions of ecosystems' structure and function must account for shifts in both precipitation and evaporative demand, and our identification here of the general relationship between plant water use and aridity provides a concise framework, consistent with current observations of the biosphere's reaction to changing climate.

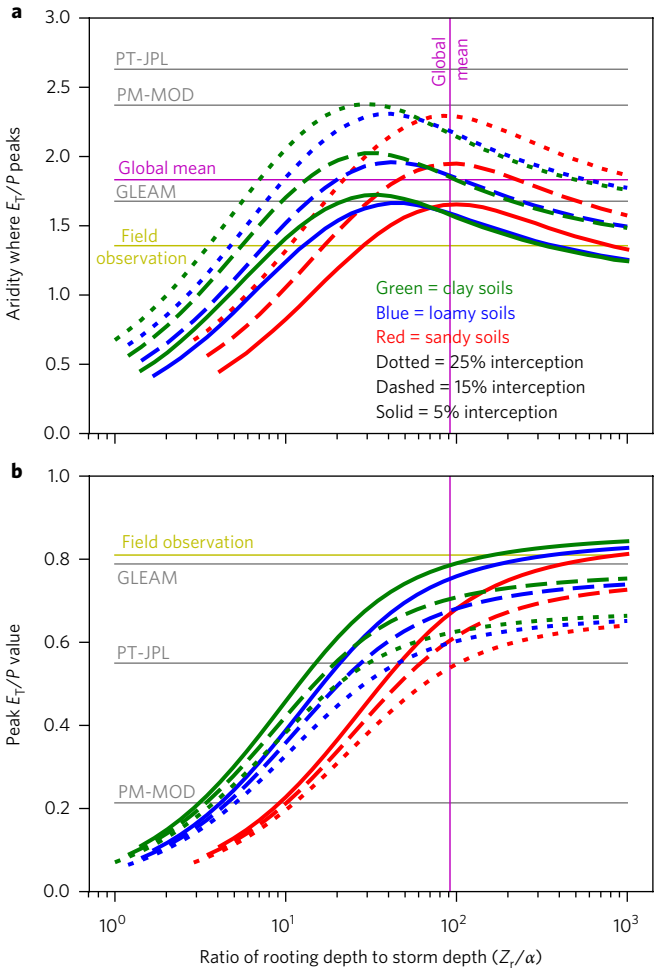

Fig. 2 | Peak plant water use across possible soil, climate and vegetation structures. a, Aridity value where E_T/P peaks for different soil types and interception values, with soil properties and wilting points from the literature[31]. **b**, The value of E_T/P at its peak increases in a sigmoidal fashion with the ratio of the effective rooting depth (Z_r) to storm depth (α). The ratio of the global average rooting depth[34] of 67.8 cm and storm depth[33] of 7.4 mm is shown as a vertical magenta line in **a** and **b**. The average global aridity value[35] of 1.8 is shown as a horizontal magenta line in **a**. Derived values from field observations, the PM-MOD algorithm, GLEAM and the PT-JPL algorithm[23] are shown as horizontal lines in **a** and **b**.

Methods

Datasets used. The field-based observations originated from published studies spanning the 1970s to 2014 (see Supplementary Table 1). These studies are primarily based on annual scale estimates and are assumed to represent steady-state conditions for each location. The compilation of Schlesinger and Jasechko[20] was used as an initial starting point, although many of these locations were excluded as they did not meet our standards due to incomplete data (we required both E_T and E_S, latitude and longitude coordinates, as well as E_A), heavy vegetation management (for example, agriculture) or quality concerns (for example, if E_A/P was reported as greater than 1 or if no observation of vegetation was used in the partitioning such that these estimates were purely a modelled result or solely based on groundwater or surface water). To these, additional studies found in the literature were added, to represent the widest possible range of P and best available estimates of E_T at the stand scale. For each field site, the aridity index was derived from local P reported in the literature and E_p from the CGIAR Consortium for Spatial Information Global Aridity and Global Potential Evapo-Transpiration Database[35] (http://www.cgiar-csi.org/).

The satellite-based evapotranspiration datasets were developed within the Water Cycle Multi-mission Observation Strategy—EvapoTranspiration project[23] and are available via http://wacmoset.estellus.eu. The three datasets were produced by running the corresponding models using a common forcing dataset mostly composed of satellite-observable variables. The PM-MOD model is based on the Penman–Monteith equation. The parameterizations of aerodynamic and surface resistances for each component of evaporation are based on extending biome-specific conductance parameters to the canopy scale using vegetation phenology and meteorological data. The model applies a surface resistance

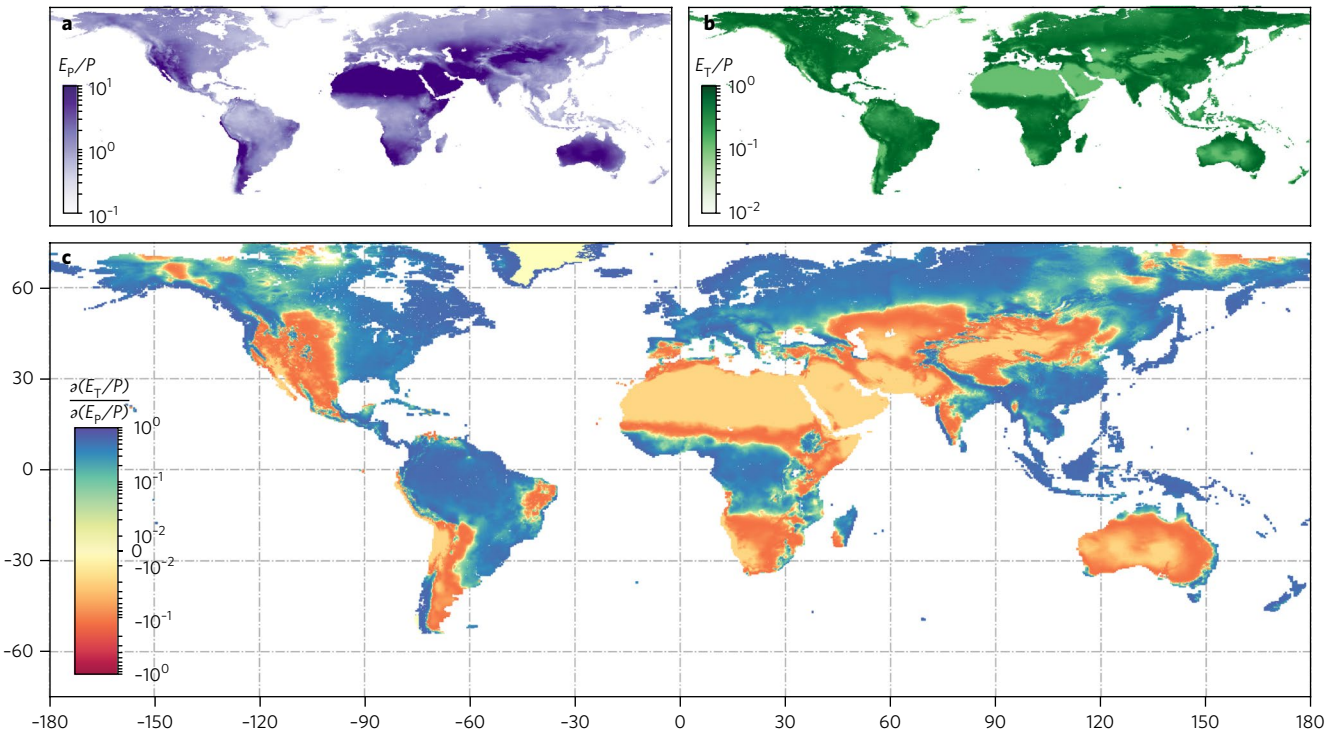

Fig. 3 | Spatial patterns in aridity, transpiration and their inter-related sensitivity. a, Global map of aridity from ref. [35]. **b**, Biological component of the hydrological cycle. **c**, Change in E_T/P expected for a change in aridity (E_P/P). Maps **b** and **c** are based on the average conditions modelled in Fig. 1c for E_P/P values from **a**.

scheme that uses the leaf area index, vapour pressure deficit and minimum temperature. GLEAM is a simple land surface model fully dedicated to deriving evaporation. Interception loss is independently calculated based on a Gash analytical model. The remaining evapotranspiration components are based on the formulation by Priestley and Taylor constrained by observations of the content of water in vegetation, precipitation and surface soil moisture. Finally, the PT-JPL model uses the Priestley and Taylor approach to estimate E_P, but unlike GLEAM, it applies a series of empirical stress factors based on the vapour pressure deficit, relative humidity and optical vegetation indices to constrain these estimates. The partitioning between transpiration and interception is done using a threshold based on relative humidity.

Minimalistic ecohydrology model. At the daily timescale, the change in soil moisture, s, within a column with roots of depth, Z_r, and porosity, n, is determined as the balance of input precipitation, and losses to runoff, (including downward leakage), interception, soil evaporation, and transpiration as

$$nZ_r\frac{ds}{dt} = P[t] - E_S[s(t)] - E_T[s(t)] - E_I[t] - Q[s(t), t] \quad (1)$$

where the variables are a function of time t, soil moisture content, $s(t)$, or both. Through the representation of P as a marked Poisson process, characterized by the frequency, λ, and depth, α, of precipitation events (derived from the mean and variance of daily precipitation[33]), analytical solutions of the stochastic soil water balance in equation (1) have previously been determined[30]. These simplified solutions have demonstrated the importance of various controlling parameters (for example, λ, α, n, Z_r) on hydrological dynamics across a wide range of studies and provide a theoretical foundation for the empirical function derived by Budyko[30]. Applying dimensional analysis to the hydrological cycle, four parameters can be used to describe the partitioned water balance: (1) the aridity index $\phi = E_P/P$, (2) the ratio of soil storage capacity to average rainfall intensity $\gamma = w_0/\alpha$, (3) the ratio of canopy storage to average rainfall intensity $\delta = \Delta/\alpha$ and (4) the relative soil moisture content where transpiration stops $\omega = (s_w - s_{fc})/(s_h - s_{fc})$. In these dimensionless parameters, E_P is the potential evapotranspiration and $w_0 = (s_h - s_{fc})nZ_r$ is the soil moisture holding capacity, with s_h, s_w and s_{fc} as the hygroscopic, wilting and field capacity of soil saturation.

In this study, the minimalistic stochastic water balance of Porporato et al.[30] is expanded to fully partition the water balance and examine the role of biota on hydrology across climates. Budyko's framework was derived based on hydrological partitioning under steady-state conditions[29]. Our model is evaluated on the annual timescale using annual observations and forcing data, and the effects of seasonality are not considered here. Strong seasonality in rainfall and potential evapotranspiration can alter the E_A/E_P ratio, particularly in drier climates, although some of these effects are mitigated by increased water storage associated with deeper rooting zones[39]. At the daily timescale, interception is treated as a censoring process[31] that alters the statistics of rainfall arriving at the soil surface, with events less frequent, $\lambda' = \lambda e^{-\delta}$. Throughfall ($P'$) has been shown to scale linearly with total precipitation, and the expected below-canopy average rainfall depth (α') is represented as being proportional to the initial average depth[40] as $\alpha' = k_I\,\alpha$, with k_I taken to be $(1-\delta)$. The average throughfall fraction, P'/P, is then $\alpha'\lambda'/\alpha\lambda = (1-\delta)e^{-\delta}$, with δ defined between 0 and 1.

Similar to the energy limit within the Budyko framework ($E_A \le E_P$), on average, interception cannot exceed the evaporative capacity of the atmosphere ($E_I \le E_P$ since E_I is a subcomponent of E_A). Because the evaporation of intercepted water requires energy, we assume here that some of the evaporative potential of the atmosphere is consumed by E_I. The soil then experiences a slightly decreased potential evaporation, as $E_P' = E_P - E_I$. Our approach is only valid when the average potential evapotranspiration is greater than the average interception and, as a consequence, if δ is held constant (unlikely), when E_P becomes very small (below all our observed data points), E_I makes up the entirety of E_A, as shown on the left edge of Supplementary Fig. 3. Importantly, because of interception, the soil also experiences an altered dryness index, $\phi' = E_P'/P' = (\phi - 1 + (1-\delta)e^{-\delta})/((1-\delta)e^{-\delta})$ and γ value, $\gamma' = \gamma/(1-\delta)$, than would occur without a vegetation canopy.

Evapotranspiration from the soil ($E_T + E_S$) is treated as decreasing linearly from the maximum potential amount (E_P) at s_{fc} to 0 when the soil is at s_h. Although evapotranspiration is known to be nonlinear at point-scales, temporal variation and spatial heterogeneity in hydrological processes at regional scales work to linearize soil moisture losses[30] and this simplification is again used here. By defining the relative 'effective' soil moisture, $x = (s - s_h)/(s_{fc} - s_h)$, the probability density function of relative soil moisture, $p(x)$, is given by a truncated gamma distribution as

$$p(x) = \frac{x^{\frac{\gamma'}{\phi'}-1}e^{-\gamma' x}\gamma'^{\frac{\gamma'}{\phi'}}}{\Gamma\left(\frac{\gamma'}{\phi'}\right) - \Gamma\left(\frac{\gamma'}{\phi'}, \gamma'\right)} \quad (2)$$

where $\Gamma(\bullet)$ and $\Gamma(\bullet,\bullet)$ are the complete and upper incomplete gamma functions, respectively. Soil moisture losses through evapotranspiration therefore scale with x, as $(E_T + E_S) = xE_P$. Equation (2) differs slightly from that originally derived by ref. [30] because ϕ' and γ' now account for interception losses.

Below the relative effective wilting point, ω, all evapotranspiration losses from the soil column are attributed to soil surface evaporation, as vegetation no longer removes water from the soil column. Above this point, any increase in soil moisture results in increased transpiration; that is, $E_T = (x-\omega)E_p$ for $x > \omega$ and $E_T = 0$ otherwise. Ground surface evaporation losses are constant at ωE_p when the relative soil moisture is above the wilting point, and $E_S = xE_p$ when $x < \omega$. This effectively splits ground surface evaporation into stage I and stage II soil moisture losses[41], with an atmospheric limited stage I (constant at $E_S = \omega E_p$) and soil limited stage II (decaying from ωE_p to zero as soil moisture falls below ω). A consequence of this approach is that once soils are wet enough for vegetation to transpire, soil surface evaporation ceases to increase as soil moisture increases. While it is possible that soil surface evaporation may continue to increase, remain constant (as modelled here) or decrease (unlikely) as relative soil moisture rises above the wilting point, specification of this additional slope adds complexity for which limited observations are available to support parameterization. A constant, atmosphere controlled soil surface evaporation rate[41] when soil moisture is above the wilting point, with the transition from stage I to stage II occurring at the wilting point, is a parsimonious approach, and further studies should explore this transition point and slope in detail.

Because E_S is constant above ω, the fraction of evapotranspiration leaving the soil as transpiration, $f = E_T/(E_T + E_S)$, is simply the ratio $(x-\omega)/x$ for relative soil moisture values above ω. The expected ratio of transpiration to evaporation plus transpiration can be calculated directly as

$$f = \int_{\omega}^{1} p(x)\left(\frac{x-\omega}{x}\right)\mathrm{d}x = \frac{\left[\Gamma\left(\frac{\gamma'}{\phi'}, \gamma'\omega\right) - \Gamma\left(\frac{\gamma'}{\phi'}, \gamma'\right)\right] - \omega\gamma'\left[\Gamma\left(\frac{\gamma'}{\phi'}-1, \gamma'\omega\right) - \Gamma\left(\frac{\gamma'}{\phi'}-1, \gamma'\right)\right]}{\Gamma\left(\frac{\gamma'}{\phi'}\right) - \Gamma\left(\frac{\gamma'}{\phi'}, \gamma'\right)} \quad (3)$$

Note, that the denominator in the definition of f does not include interception. The average soil moisture can also be calculated directly as

$$\overline{x} = \frac{1}{\phi'} - \frac{\gamma'^{\frac{1}{\phi'}}}{\Gamma\left(\frac{\gamma'}{\phi'}\right) - \Gamma\left(\frac{\gamma'}{\phi'}, \gamma'\right)} \quad (4)$$

The average fraction of throughfall leaving the system as either ground surface evaporation or transpiration is equal to $\overline{x}\phi'$. Again, equation (4) differs slightly from that derived by ref. [30] because ϕ' and γ' account for interception losses. The portion of precipitation that exits the system as runoff and interception can then be estimated as

$$\frac{Q}{P} = (1-\overline{x}\phi')(1-\delta)\mathrm{e}^{-\delta} \quad (5)$$

and

$$\frac{E_I}{P} = 1-(1-\delta)\mathrm{e}^{-\delta} \quad (6)$$

In equation (5), $1-\overline{x}\phi'$ is the throughfall fraction leaving as runoff, Q/P', and $(1-\delta)\mathrm{e}^{-\delta}$ is P'/P. Finally, we can calculate the fraction of input precipitation that exits the system as ground surface evaporation and transpiration as

$$\frac{E_S}{P} = (1-f)\overline{x}\phi'(1-\delta)\mathrm{e}^{-\delta} \quad (7)$$

and

$$\frac{E_T}{P} = f\,\overline{x}\phi'(1-\delta)\mathrm{e}^{-\delta} \quad (8)$$

where $\overline{x}\phi'$ is the ratio of $(E_S + E_T)/P'$ and $(1-\delta)\mathrm{e}^{-\delta}$ is P'/P. Equations (5), (6), (7) and (8) represent a generalized theory of how input precipitation is partitioned by the characteristic of climate (ϕ, λ and α), soil (n and ω) and vegetation properties (Z_r and Δ).

Life Sciences Reporting Summary. Further information on experimental design and reagents is available in the Life Sciences Reporting Summary.

Data availability. Field observations of evapotranspiration components were compiled from previously published literature and are included in Supplementary Table 1. The remote sensing datasets used here may be obtained from the Water Cycle Multi-mission Observation Strategy—EvapoTranspiration project[23] at http://wacmoset.estellus.eu

Received: 5 April 2017; Accepted: 9 October 2017;

References

1. Berg, A. et al. Land–atmosphere feedbacks amplify aridity increase over land under global warming. *Nat. Clim. Change* **6**, 869–874 (2016).
2. Polson, D. & Hegerl, G. C. Strengthening contrast between precipitation in tropical wet and dry regions. *Geophys. Res. Lett.* **44**, 365–373 (2017).
3. Caylor, K. K., Scanlon, T. M., Rodriguez-Iturbe, I. & Rodríguez-Iturbe, I. Ecohydrological optimization of pattern and processes in water-limited ecosystems: a trade-off-based hypothesis. *Water Resour. Res.* **45**, W08407 (2009).
4. Haddeland, I. et al. Global water resources affected by human interventions and climate change. *Proc. Natl Acad. Sci. USA* **111**, 3251–3256 (2014).
5. Cheng, L. et al. Recent increases in terrestrial carbon uptake at little cost to the water cycle. *Nat. Commun.* **8**, 110 (2017).
6. Del Grosso, S. et al. Global potential net primary production predicted from vegetation class, precipitation, and temperature. *Ecology* **89**, 2117–2126 (2008).
7. Huxman, T. E. et al. Convergence across biomes to a common rain-use efficiency. *Nature* **429**, 651–654 (2004).
8. Bruijnzeel, L. A. & Veneklaas, E. J. Climatic conditions and tropical montane forest productivity: the fog has not lifted yet. *Ecology* **79**, 3–9 (1998).
9. Schuur, E. A. G. Productivity and global climate revisited: the sensitivity of tropical forest growth to precipitation. *Ecology* **84**, 1165–1170 (2003).
10. Smith, W. K. & McClean, T. M. Adaptive relationship between leaf water repellency, stomatal distribution, and gas exchange. *J. Chem. Inf. Model.* **96**, 465–469 (1989).
11. Taylor, P. G. et al. Temperature and rainfall interact to control carbon cycling in tropical forests. *Ecol. Lett.* **20**, 779–788 (2017).
12. Zhu, K., Chiariello, N. R., Tobeck, T., Fukami, T. & Field, C. B. Nonlinear, interacting responses to climate limit grassland production under global change. *Proc. Natl Acad. Sci. USA* **113**, 10589–10594 (2016).
13. Sala, O. E., Parton, W. J., Joyce, L. A. & Lauenroth, W. K. Primary production of the central grassland region of the United States. *Ecology* **69**, 40–45 (1988).
14. Mueller, K. E., Tilman, D., Fornara, D. A. & Hobbie, S. E. Root depth distribution and the diversity–productivity relationship in a long-term grassland experiment. *Ecology* **94**, 787–793 (2013).
15. Good, S. P. & Caylor, K. K. Climatological determinants of woody cover in Africa. *Proc. Natl Acad. Sci. USA* **108**, 4902–4907 (2011).
16. Vicente-Serrano, S. M. et al. Response of vegetation to drought time-scales across global land biomes. *Proc. Natl Acad. Sci. USA* **110**, 52–57 (2013).
17. Yang, Y. et al. Contrasting responses of water use efficiency to drought across global terrestrial ecosystems. *Sci. Rep.* **6**, 23284 (2016).
18. Bonell, M. Possible impacts of climate variability and change on tropical forest hydrology. *Clim. Change* **39**, 215–272 (1998).
19. Foster, P. The potential negative impacts of global climate change on tropical montane cloud forests. *Earth-Sci. Rev.* **55**, 73–106 (2001).
20. Schlesinger, W. H. & Jasechko, S. Transpiration in the global water cycle. *Agric. For. Meteorol.* **189–190**, 115–117 (2014).
21. Wang, L., Good, S. P. & Caylor, K. K. Global synthesis of vegetation control on evapotranspiration partitioning. *Geophys. Res. Lett.* **41**, 6753–6757 (2014).
22. Good, S. P., Noone, D. & Bowen, G. Hydrologic connectivity constrains partitioning of global terrestrial water fluxes. *Science* **349**, 175–177 (2015).
23. Miralles, D. G. et al. The WACMOS-ET project—part 2: evaluation of global terrestrial evaporation data sets. *Hydrol. Earth Syst. Sci.* **20**, 823–842 (2016).
24. Wang, L. et al. The effect of warming on grassland evapotranspiration partitioning using laser-based isotope monitoring techniques. *Geochim. Cosmochim. Acta* **111**, 28–38 (2013).
25. Wei, Z. et al. Revisiting the contribution of transpiration to global terrestrial evapotranspiration. *Geophys. Res. Lett.* **44**, 2792–2801 (2017).
26. Gibson, J. J. & Edwards, T. W. D. Regional water balance trends and evaporation—transpiration partitioning from a stable isotope survey of lakes in northern Canada. *Glob. Biogeochem. Cycles* **16**, 10–11 (2002).
27. Maxwell, R. M. & Condon, L. E. Connections between groundwater flow and transpiration partitioning. *Science* **353**, 377–380 (2016).
28. Moore, G. W. & Heilman, J. L. Proposed principles governing how vegetation changes affect transpiration. *Ecohydrology* **4**, 351–358 (2011).
29. Budyko, M. I. *Climate and Life* (Academic Press, New York, NY, 1974).
30. Porporato, A., Daly, E. & Rodríguez-Iturbe, I. Soil water balance and ecosystem response to climate change. *Am. Nat.* **164**, 625–632 (2004).
31. Laio, F., Porporato, A., Ridolfi, L., Rodríguez-Iturbe, I. & Ridol, L. Plants in water-controlled ecosystems: active role in hydrologic processes and response to water stress: II. Probabilistic soil moisture dynamics. *Adv. Water Resour.* **24**, 707–723 (2001).

32. Wang, D., Wang, G. & Anagnostou, E. N. Evaluation of canopy interception schemes in land surface models. *J. Hydrol.* **347**, 308–318 (2007).
33. Good, S. P., Guan, K. & Caylor, K. K. Global patterns of the contributions of storm frequency, intensity, and seasonality to interannual variability of precipitation. *J. Clim.* **29**, 3–15 (2016).
34. Yang, Y., Donohue, R. J. & McVicar, T. R. Global estimation of effective plant rooting depth: implications for hydrological modeling. *Water Resour. Res.* **52**, 8260–8276 (2016).
35. Zomer, R. J., Trabucco, A., Bossio, D. A. & Verchot, L. V. Climate change mitigation: a spatial analysis of global land suitability for clean development mechanism afforestation and reforestation. *Agric. Ecosyst. Environ.* **126**, 67–80 (2008).
36. Roderick, M. L., Sun, F., Lim, W. H. & Farquhar, G. D. A general framework for understanding the response of the water cycle to global warming over land and ocean. *Hydrol. Earth Syst. Sci.* **18**, 1575–1589 (2014).
37. Byrne, M. P., O'Gorman, P. A., Byrne, M. P. & O'Gorman, P. A. The response of precipitation minus evapotranspiration to climate warming: why the 'wet-get-wetter, dry-get-drier' scaling does not hold over land. *J. Clim.* **28**, 8078–8092 (2015).
38. Wu, H.-T. J. & Lau, W. K.-M. Detecting climate signals in precipitation extremes from TRMM (1998–2013)—increasing contrast between wet and dry extremes during the 'global warming hiatus'. *Geophys. Res. Lett.* **43**, 1340–1348 (2016).
39. Feng, X., Vico, G. & Porporato, A. On the effects of seasonality on soil water balance and plant growth. *Water Resour. Res.* **48**, W05543 (2012).
40. Daly, E., Oishi, A. C., Porporato, A. & Katul, G. G. A stochastic model for daily subsurface CO_2 concentration and related soil respiration. *Adv. Water Resour.* **31**, 987–994 (2008).
41. Salvucci, G. D. Soil and moisture independent estimation of stage-two evaporation from potential evaporation and albedo or surface temperature. *Water Resour. Res.* **33**, 111–122 (1997).

Acknowledgements

S.P.G. acknowledges the financial support of the Unites States National Aeronautics and Space Administration (NNX16AN13G). G.W.M. acknowledges the United States Department of Energy Biological and Environmental Research programme at the Office of Science for financial support (DE-SC0010654). D.G.M. acknowledges support from the European Research Council under grant agreement number 715254 (DRY-2-DRY). We acknowledge A. Jaimes for assistance with data analysis. We also acknowledge K. Caylor, L. Wang and I. Rodriguez-Iturbe for some early suggestions on this work.

Author contributions

S.P.G. designed the study with input from G.W.M. and D.G.M. S.P.G. and G.W.M. compiled the field observations. S.P.G. and D.G.M. provided the remote-sensing-based observations. S.P.G. conducted the minimalistic model simulations. All authors wrote the paper.

Competing interests

The authors declare no competing financial interests.

Additional information

Supplementary information is available for this paper at https://doi.org/10.1038/s41559-017-0371-8.

Reprints and permissions information is available at www.nature.com/reprints.

Correspondence and requests for materials should be addressed to S.P.G.

Publisher's note: Springer Nature remains neutral with regard to jurisdictional claims in published maps and institutional affiliations.

nature ecology & evolution

SUPPLEMENTARY INFORMATION

https://doi.org/10.1038/s41559-017-0371-8

In the format provided by the authors and unedited.

A mesic maximum in biological water use demarcates biome sensitivity to aridity shifts

Stephen P. Good[1]*, Georgianne W. Moore[2] and Diego G. Miralles[3]

[1]Department of Biological and Ecological Engineering, Oregon State University, Corvallis, OR, USA. [2]Department of Ecosystem Science and Management, Texas A&M University, College Station, TX, USA. [3]Laboratory of Hydrology and Water Management, Ghent University, Ghent, Belgium. *e-mail: stephen.good@oregonstate.edu

Supplementary Table 1 | Compiled field observations of water fluxes.

Biome	*P*	*T*	*ET*	*T:ET*	*ET:P*	*PET*	*PET:P*	*T:P*	Methods	Source
Cloud Forest	7471	349	898	0.39	0.12	1392	0.19	0.05	Sapflow	McJannet et al 2007[1]
Cloud Forest	5303	349	910	0.38	0.17	1504	0.28	0.07	Sapflow + other	McJannet et al 2007[2]
Cloud Forest	4450	484	674	0.72	0.15	1350	0.30	0.11	Micromet	Ataroff and Rada 2000[3]
Cloud Forest	3040	579	1459	0.40	0.48	1445	0.48	0.19	Sapflow	McJannet et al 2007a
Cloud Forest	2983	591	1445	0.41	0.48	1461	0.49	0.20	Sapflow	McJannet et al 2007a
Cloud Forest	1768	626	812	0.77	0.46	1616	0.91	0.35	Sapflow	Tanaka et al 2011[4]
Tropical Montane	4200	540	1004	0.54	0.24	1523	0.36	0.13	Sapflow, models	Aparecido et al 2016[5]
Tropical Montane	2833	579	882	0.66	0.31	1445	0.51	0.20	Sapflow + other	McJannet et al 2007b
Tropical Montane	2420	591	1087	0.54	0.45	1461	0.60	0.24	Sapflow + other	McJannet et al 2007b
Lowland Tropical	2851	884	1483	0.60	0.52	1675	0.59	0.31	Model (with met. data)	Schlesinger and Jasechko 2014[6]
Lowland Tropical	2740	1193	1545	0.77	0.56	1486	0.54	0.44	Models	Kumagai et al 2005[7]
Lowland Tropical	2484	587	1143	0.51	0.46	1502	0.60	0.24	Sapflow + other	McJannet et al 2007b
Lowland Tropical	2232	893	1116	0.80	0.50	1605	0.72	0.40	Model (with met. data)	Schlesinger and Jasechko 2014
Lowland Tropical	2209	1237	1480	0.84	0.67	1609	0.73	0.56	Model (with met. data)	Schlesinger and Jasechko 2014
Lowland Tropical	2209	1244	1495	0.83	0.68	1613	0.73	0.56	Model (with met. data)	Leopoldo et al 1995[8]
Lowland Tropical	2000	980	1500	0.65	0.75	1605	0.80	0.49	Model (with met. data)	Schlesinger and Jasechko 2014
Lowland Tropical	2000	1240	1620	0.77	0.81	1605	0.80	0.62	Model (with met. data)	Schlesinger and Jasechko 2014
Lowland Tropical	1623	730	1639	0.45	1.01	1634	1.01	0.45	-	Schlesinger and Jasechko 2014
Lowland Tropical	1571	1218	1548	0.79	0.99	1685	1.07	0.78	Model (with met. data)	Tani et al 2003[9]
Lowland Tropical	1019	825	948	0.87	0.93	1382	1.36	0.81	Radial flow meter	Schlesinger and Jasechko 2014
Temperate	3482	90	225	0.39	0.20	886	0.25	0.03	Sap flow	Schlesinger and Jasechko 2014
Temperate	2620	183	786	0.23	0.30	586	0.22	0.07	Model (with met. data)	Schlesinger and Jasechko 2014
Temperate	2128	486	911.4	0.53	0.43	1122	0.53	0.23	Model (with met. data), sap flow	Schlesinger and Jasechko 2014
Temperate	1333	253	440	0.58	0.33	1237	0.93	0.19	Model (with met. data), sap flow	Schlesinger and Jasechko 2014
Temperate	1085	532	694	0.76	0.64	1637	1.51	0.49	Modelled (no observations)	Schlesinger and Jasechko 2014
Temperate	763	252	366	0.69	0.48	787	1.03	0.33	Sap flow	Schlesinger and Jasechko 2014
Temperate	725	268	428	0.63	0.59	767	1.06	0.37	Energy balance model	Schlesinger and Jasechko 2014
Temperate	627	251	552	0.41	0.88	747	1.19	0.40	-	Schlesinger and Jasechko 2014
Temperate	626	313	620	0.50	0.99	747	1.19	0.50	-	Schlesinger and Jasechko 2014
Temperate	595	351	565	0.55	0.95	658	1.11	0.59	Model (with met. data)	Schlesinger and Jasechko 2014
Temperate	549	296	346	0.86	0.63	562	1.02	0.54	Model (with met. data)	Schlesinger and Jasechko 2014
Temperate	513	251	436	0.58	0.85	798	1.56	0.49	-	Schlesinger and Jasechko 2014
Temperate	366	190	384	0.52	1.05	658	1.80	0.52	Model (with met. data)	Schlesinger and Jasechko 2014
Boreal Forest	1237	235	557	0.42	0.45	588	0.48	0.19	-	Schlesinger and Jasechko 2014
Boreal Forest	872	392	462	0.85	0.53	833	0.96	0.45	Isotope-based (catchment)	Schlesinger and Jasechko 2014
Boreal Forest	340	241	303	0.81	0.89	425	1.25	0.71	Isotope-based (catchment)	Schlesinger and Jasechko 2014
Boreal Forest	250	115	178	0.65	0.71	565	2.26	0.46	Sap flow	Schlesinger and Jasechko 2014
Grassland	1019	591	703	0.84	0.69	1382	1.36	0.58	Radial flow meter	Schlesinger and Jasechko 2014
Grassland	580	226	510	0.44	0.88	812	1.40	0.39	Model (with met. data)	Schlesinger and Jasechko 2014
Grassland	275	151	245	0.62	0.89	806	2.93	0.55	Model (with met. data)	Schlesinger and Jasechko 2014
Shrub	590	207	531	0.39	0.90	1304	2.21	0.35	Model (with met. data)	Schlesinger and Jasechko 2014
Shrub	475	152	394	0.39	0.83	1188	2.50	0.32	Model (with met. data)	Schlesinger and Jasechko 2014
Shrub	285	128	259	0.48	0.91	1404	4.93	0.45	Model (with met. data), sap flow	Schlesinger and Jasechko 2014
Desert	260	55	148	0.42	0.57	1553	5.97	0.21	Model (with met. data), sap flow	Schlesinger and Jasechko 2014
Desert	212	45	102	0.47	0.48	1626	7.67	0.21	Model (with met. data), sap flow	Schlesinger and Jasechko 2014

[1] McJannet, D. *et al.* Measurements of transpiration in four tropical rainforest types of north Queensland, Australia. *Hydrol. Proc.* 21, 3549-3564, (2007).

[2] McJannet, D. *et al.* Water balance of tropical rainforest canopies in north Queensland, Australia. *Hydrol. Proc.* 21, 3473-3484, (2007).

[3] Ataroff, V. & Rada, F. Deforestation impact on water dynamics in a Venezuelan Andean cloud forest. *Ambio* 29, 440-444 (2000).

[4] Tanaka, N. *et al.* Relationships between rainfall, fog and throughfall at a hill evergreen forest site in northern Thailand. *Hydrol. Proc.* 25, 384-391, (2011).

[5] Aparecido, L. M. T., Miller, G. R., Cahill, A. T. & Moore, G. W. Comparison of tree transpiration under wet and dry canopy conditions in a Costa Rican premontane tropical forest. *Hydrol. Proc.* , (2016).

[6] Schlesinger, W. H. & Jasechko, S. Transpiration in the global water cycle. *Ag. and For. Met.* 189, 115-117, (2014).

[7] Kumagai, T. *et al.* Annual water balance and seasonality of evapotranspiration in a Bornean tropical rainforest. *Ag. and For. Met.* 128, 81-92, (2005).

[8] Leopoldo, P. R., Franken, W. K. & Nova, N. A. V. Real Evapotranspiration and Transpiration through a Tropical Rain-Forest in Central Amazonia as Estimated by the Water-Balance Method. *For. Ecol. and Mgmt.* 73, 185-195, (1995).

[9] Tani, M. *et al.* Long-term estimation of evapotranspiration from a tropical rain forest in Peninsular Malaysia. *Water Res. Syst.--Water Avail. Global Change* 267-274 (2003).

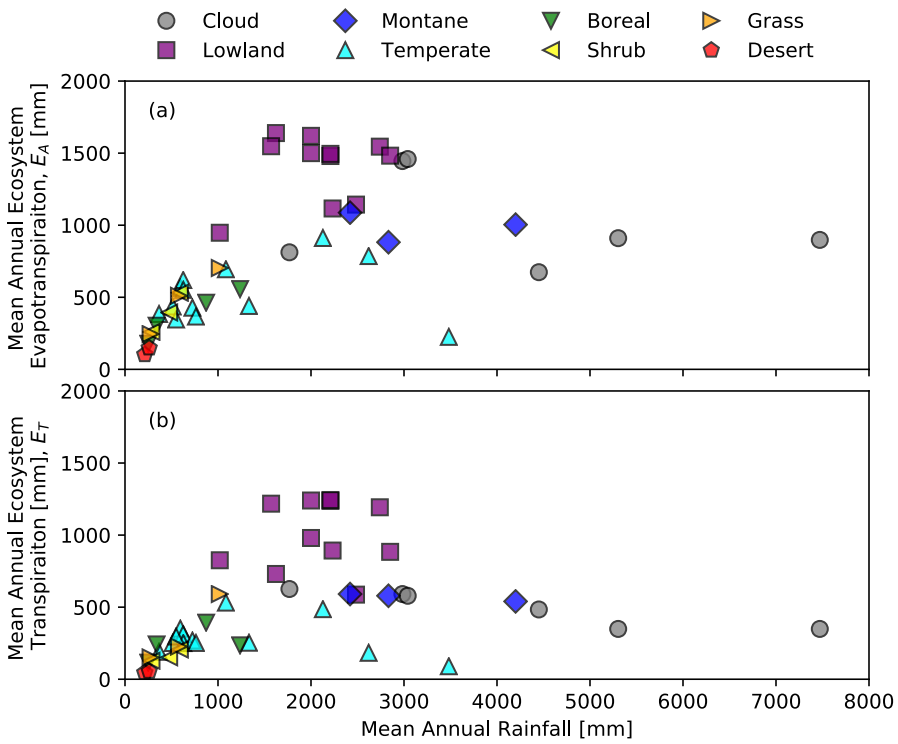

Supplementary Figure 1 | Evaporative fluxes across rainfall regimes. Based on field studies, both (a) total surface-to-atmosphere evaporation, and (b) only the transpiration, E_T exhibit a decline in water fluxes as precipitation becomes very high. Symbols and colors depict different biomes.

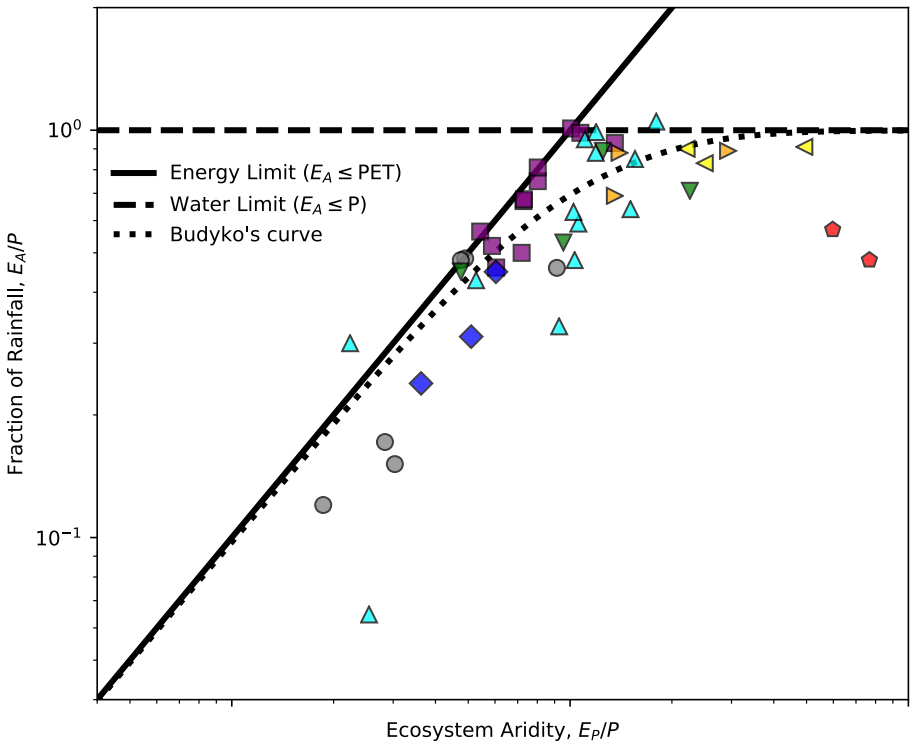

Supplementary Figure 2 | Rainfall fraction in Budyko space. The fraction of rainfall that returns to the atmosphere (E_A/P) is plotted against the ecosystem aridity. The equilibrium E_A/P ratio is primarily bound by both an energy availability limit, $E_A \leq E_P$, and a water availability limit, $E_A \leq P$, with field studies generally following the curve offered by Budyko in 1974. Symbols are the same as in Figure S1.

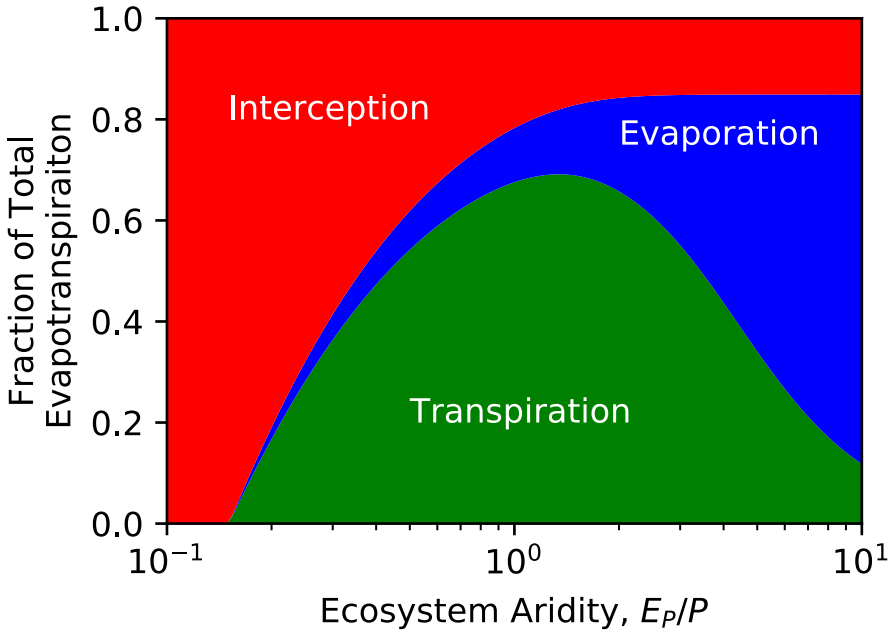

Supplementary Figure 3 | Partitioned evapotranspiration fluxes. Modeled fraction of total evapotranspiration fluxes that returns to the atmosphere as interception (red), ground surface evaporation (blue) and canopy transpiration (green), based the same model parameters as. Figure 1c. Because δ is held constant in this figure E_I exceeds E_P while E_S and E_T are zero at low aridity.

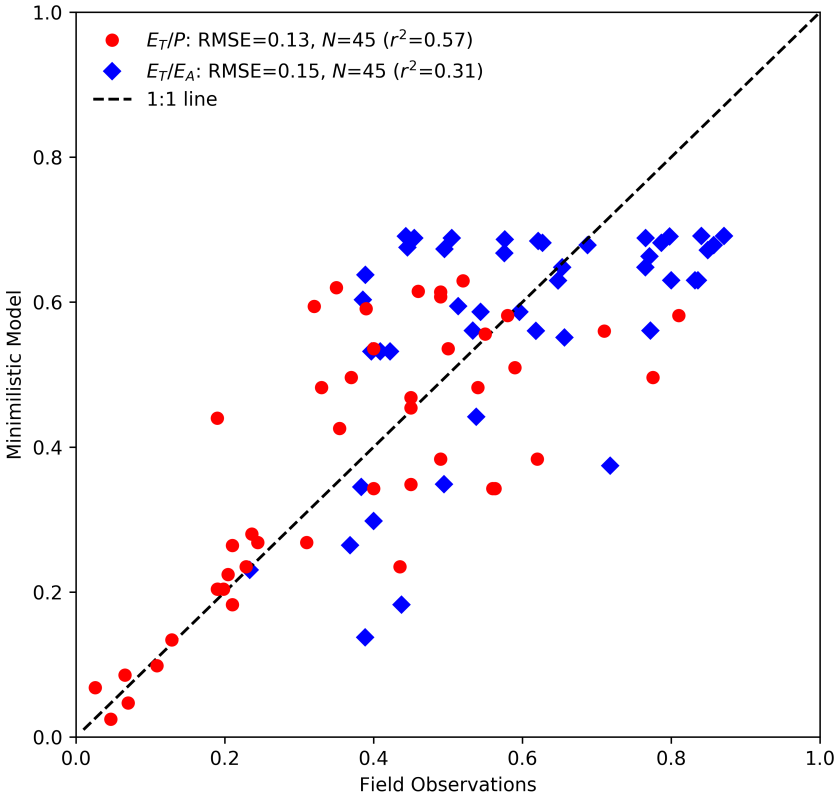

Supplementary Figure 4 | Model-observation comparison. Field observations compared with estimates from the minimalistic model with average global parameters (see main text) for both E_T/P and E_T/E_A.